Research Square

Preprints are preliminary reports that have not undergone peer review.
They should not be considered conclusive, used to inform clinical practice,
or referenced by the media as validated information.

Humanized diet and thermoneutral housing enable sex-aware dissection of the MASLD-T2D-CVD triad

Benjamin Jensen

benjamin.jensen@sund.ku.dk

University of copenhagen https://orcid.org/0000-0001-6991-0828

Sune Yang-Jensen

Department of Biomedical Sciences, Faculty of Health and Medical Sciences, University of Copenhagen, Copenhagen, Denmark

Lais Perezza

Department of Medicine, Faculty of Medicine, Cardiology Axis of the Québec Heart and Lung Institute, Laval University, Québec, Canada

Vanessa Vilela

Department of Medicine, Faculty of Medicine, Cardiology Axis of the Québec Heart and Lung Institute, Laval University, Québec, Canada

Ida Larsen

University of Copenhagen

Thorben Sauer

Laboratory for Surgical Research, Department of Surgery, University Hospital Schleswig-Holstein, Campus Lübeck, Ratzeburger Allee 160, 23562 Lübeck, Germany

Marianne Agerholm

University of Copenhagen

Bandik Foeh

Institute of Nutritional Medicine, University Hospital Schleswig-Holstein, Campus Lübeck, Lübeck, Germany

Louis Koeninger

Department of Internal Medicine I, University Hospital Tübingen, 72076 Tübingen, Germany

Patrick Mathieu

Institut universitaire de cardiologie et de pneumologie de Québec – Université Laval
https://orcid.org/0000-0002-3805-2004

Jens Jacobsen

University of Copenhagen

Felix Boel

University of Southern Denmark https://orcid.org/0000-0003-4232-8613

Patricia Mitchell

Université Laval https://orcid.org/0000-0002-0773-1047
Mathieu Laplante
Université Laval https://orcid.org/0000-0002-1752-6741
Philip Hallenborg
University of Southern Denmark
Blagoy Blagoev
University of Southern Denmark https://orcid.org/0000-0002-3596-0066
Christian Sina
Institute of Nutritional Medicine, University Hospital Schleswig-Holstein, Lübeck
Timo Gemoll
Laboratory for Surgical Research, Department of Surgery, University Hospital Schleswig-Holstein, Campus Lübeck, Ratzeburger Allee 160, 23562 Lübeck, Germany
Andre Marette
Université Laval https://orcid.org/0000-0003-3950-5973

Article

Keywords:

Posted Date: April 7th, 2026

DOI: https://doi.org/10.21203/rs.3.rs-9108360/v1

License: This work is licensed under a Creative Commons Attribution 4.0 International License.
Read Full License

Additional Declarations: There is **NO** Competing Interest.

Abstract

Metabolic dysfunction-associated steatotic liver disease (MASLD), type 2 diabetes (T2D), and cardiovascular disease (CVD) constitute a tightly interconnected axis that drives global cardiometabolic mortality. Yet their causal and temporal relationships remain difficult to disentangle. Here, we introduce a humanized mouse platform that integrates a fast-food mimicking diet (FFMD), thermoneutral housing, and genetic diversity within a sex-aware framework to resolve the hierarchy between MASLD, T2D, and CVD. FFMD feeding increases liver weight fourfold and rapidly induces severe, fully penetrant steatohepatitis (MASH) and marked hyperinsulinemia in wild-type mice, outperforming standard Western diets. Despite comparable body weight, liver fat, and liver enzymes, weight-matched diabetic db/db mice, develop MASH in only 27% of cases, compared to 100% in FFMD-fed wild-type mice, thereby uncoupling advanced liver disease from overt diabetes. Longitudinal and crossover studies in CVD-prone mice further reveal that ambient temperature dictates the transition from early MASLD to cirrhosis and aortic mineralization, implicating MASH - rather than T2D - as the main driver of advanced cardiohepatic injury. Together, this model positions ambient temperature as a tunable determinant of disease progression and provides a translational platform to interrogate and therapeutically target the MASLD-T2D-CVD triad.

Introduction

The global burden of metabolic syndrome (MetS) has reached pandemic proportions, with a reported prevalence of up to ~31% worldwide, depending on diagnostic criteria[1]. MetS comprises a cluster of interrelated metabolic risk factors that markedly increase the risk of type 2 diabetes (T2D) and cardiovascular disease (CVD)[2]. Within this cluster, metabolic dysfunction-associated steatotic liver disease (MASLD) represents the hepatic manifestation of MetS, and its progressive inflammatory form, metabolic dysfunction-associated steatohepatitis (MASH), frequently co-occurs with obesity, T2D, and cardiovascular complications[2,3]. Despite this extensive clinical overlap, the hierarchical and temporal relationships among these conditions remain poorly defined, underscoring the need to unravel the mechanisms linking this disease triad. Progress in this area is hindered by the lack of preclinical models that faithfully recapitulate the full spectrum of human cardiometabolic pathology.

Although recent advances in rodent models of MASLD, including omics-based approaches, have improved translatability[4,5], most models still fail to mimic the human aetiology of MASLD and require prolonged experimental durations (>50 weeks). They also frequently lack key histopathological features of advanced MASH, such as bridging fibrosis and hepatocellular hypertrophy[5]. Chemical- or nutrient-deficient models, although capable of producing advanced liver disease[5], deviate substantially from the lifestyle-driven aetiology observed in humans and often lack concurrent MetS features. Likewise, prevailing diet-induced obesity (DIO) models do not reflect the complexity of human dietary intake or metabolic homeostasis, limiting our ability to dissect the dietary, causal, and temporal relationships within the MASLD-T2D-CVD triad.

Unlike humans, who live near their thermoneutral zone in climate-controlled environments and adapt clothing to ambient temperature, mice housed at standard room temperature (T22, ~20-22^{o}C) experience chronic mild cold-stress that activates sympathetic thermogenesis and profoundly alters energy balance and immune function[6–8]. This rodent-specific stressor, largely absent in humans, can mask - or even invert - cardiometabolic disease phenotypes[6]. Housing mice at thermoneutrality (T30, ~28-30^{o}C) instead aligns husbandry conditions with the murine thermoneutral zone and removes this experimental artefact rather than recreating human ambient temperature or exaggerating disease. Eliminating cold-induced metabolic compensation improves alignment with the human basal metabolic rate[9], unmasks immunometabolic dysfunction[10] and yields liver pathology more reminiscent of human MASLD/MASH[11]. Thermoneutrality is equally critical for cardiovascular research; at T22, wild-type (WT) mice are generally protected from diet-induced atherosclerosis, whereas T30 restores susceptibility with lipid profiles and plaque morphology that better reflect human CVD[11,12]. Thus, thermoneutral housing reduces species-specific thermal confounders and enhances translational relevance by allowing biologically meaningful metabolic, hepatic, and cardiovascular phenotypes to emerge.

In this study, we present a mouse model specifically designed to dissect the complex relationships among T2D, MASLD, and CVD in a more human-relevant context. We demonstrate that combining our ‘humanized’ fast food-mimicking diet (FFMD) with thermoneutral housing in a dyslipidaemic background not only accelerates MASLD/MASH development but also uncouples T2D from advanced cardiohepatic disease trajectories in a sex-aware manner. Disentangling this triad is clinically important, as MASLD populations experience excess mortality largely driven by CVD, highlighting the need to define which components of the axis are causal disease targets versus correlated comorbidities. We demonstrate that our FFMD induces robust and fully penetrant liver pathology that develops independently of overt diabetes. Using CVD- and T2D-prone LDLr$^{-/-}$/ApoB$^{100/100}$/IGF-II mice[13–15] (hereafter referred to as IGFII mice), we mechanistically interrogate the hierarchy of this disease triad by modulating ambient temperature. Longitudinal and crossover experiments reveal linear relationships between ambient temperature and cardiohepatic disease severity and uncover pronounced sex differences in glucose homeostasis. At the mechanistic level, hepatic proteomics identifies diet- and temperature-dependent immune, fibrotic, and tumour-associated programs. Together, this model provides a translational platform for interrogating and therapeutically targeting the MASLD–T2D–CVD axis.

Results

Tailoring Diet to Target MASH

To target liver pathology, we designed a nutritionally complex “humanized” fast food-mimicking diet (FFMD)[16] with a fructose-to-glucose ratio resembling sugar-sweetened beverages[17,18]. While presenting macronutrient proportions similar to traditional Western diets (WD) for rodents, our customized FFMD diverges by integrating diverse protein sources, atherogenic fats, physiologically relevant cholesterol levels, and sugar-sweetened soft drinks-related carbohydrates (Figure S1A, Table S1).

To evaluate diet-dependent disease trajectories, we first compared our FFMD with an eucaloric WD in male C57BL/6J mice housed under standard T22 conditions. Non-obese reference mice were fed processed low-fat diets (LFDs), matched to each obesogenic diet (Figure 1A, S1A, Table S1). Compared to their WD-fed counterparts, FFMD-fed mice exhibited accelerated body weight gain and fat accretion (Figure S1B-C) alongside a nominal increase in energy intake (Figure S1D). This culminated in greater terminal body weight and total fat mass in FFMD-fed mice compared to WD-fed mice (Figure 1B-C). Enhanced fat deposition aligned well with compromised glucoregulatory capacity. While both obesogenic diets comparably elevated fasting blood glucose levels (Figure 1D), FFMD-fed mice exhibited pronounced hyperinsulinemia with a ~3-fold increase compared to their WD-fed counterparts (Figure 1E). These metabolic abnormalities resulted in an impaired capability of FFMD-fed mice to normalize their blood glucose after an oral glucose tolerance test (oGTT) (Figure 1F), paralleled by a vastly increased glucose-stimulated insulin secretion (GSIS), indicative of severe insulin resistance (Figure 1G). To explore this hypothesis, we turned our attention towards leptin receptor-deficient (*db/db*), diabetes-prone mice fed a standard chow diet until reaching matching weights with the WT FFMD-fed mice (10 weeks, Figure 1P-Q). Despite being weight-matched, *db/db* mice accrued more total body fat than WT FFMD-fed mice (Figure 1C, 1R). Still, the well-described impairments of glucoregulatory capacity in *db/db* mice (Figure 1S-T) closely mirrored that observed for FFMD-fed WT mice (Figure 1F-G), hence supporting a prediabetic state even in WT mice fed FFMD for 12 weeks.

Because T2D is closely associated with liver dysfunction, and the glucose-to-fructose ratio used in this study was predicted to preferably enhance liver fat, we next evaluated the livers of WT mice fed either FFMD or standard WD and compared these to the livers of diabetic *db/db* mice. We observed a ~4-fold increase in liver mass of FFMD-fed WT mice compared to their WD-fed counterparts (Figure 1H). This substantial increase exceeded that of weight-matched *db/db* mice despite their increased organismal adiposity (Figure 1U), supporting a substantial liver preference in fat partitioning of FFMD-consuming mice, as also demonstrated by relative mass of fat depots across cohorts (Figure S1E-F).

Biochemical analyzes demonstrated a clear dichotomy between the obesogenic diets in terms of circulating versus deposited fat species. In the liver, FFMD-fed WT mice exhibited a more than 3-fold increase in triacylglyceride (TAG) levels (Figure 1I), whereas hepatic cholesterol levels were not notably different between the obesogenic diets (Figure 1J). However, both circulating plasma TAG and circulating cholesterol were nearly doubled in FFMD-fed mice (Figure 1K-L), suggesting alterations in lipid handling not attributable to dietary cholesterol content alone (Table S1), which may predispose them to elevated CVD risk. Of note, and in accordance with previous reports[19], *db/db* mice exhibited a significantly altered lipid metabolism, where hepatic, but not plasma, cholesterol was magnitudes higher than *db/+* control mice as well as WD- and FFMD-fed WT mice (Figure 1V, S1G). Despite these discrepancies in hepatic cholesterol levels between insulin-resistant WT mice and diabetic *db/db* mice, plasma ALT levels suggested equally severe liver damage between FFMD-fed WT and diabetic *db/db* mice, exceeding that of any other group by nearly 10-fold (Figure 1M, 1W). Similarly, plasma and hepatic TAG was comparable between FFMD-fed WT and diabetic *db/db* mice (Figure 1I, 1K, S1H-I).

Still, upon histological assessment, FFMD-fed mice presented a unique liver phenotype suggesting divergent disease pathology (Figure 1N-O, 1X-Y). FFMD-fed mice exhibited extensive macro- and microvesicular steatosis and pronounced hepatocellular hypertrophy, features characteristic of human MASH[20] (Figure 1N-O). Severe hypertrophy (defined as >66% of liver area) and maximal steatosis and MASH grades were present in **100%** of FFMD-fed mice (Figure 1N-O). This pronounced trait was only mirrored in 6 (hypertrophy) and 3 (maximal steatosis) out of 11 weight-matched db/db mice and 0/12 WD-fed WT mice (Figure 1N, 1X), further advocating a diet-dependent, liver-specific phenotype. Histopathological assessment further revealed pronounced inflammation in 100% FFMD-fed mice (1 to 3 inflammatory foci/1mm^2); sharply contrasting the benign inflammation observed in both WD-fed counterparts and weight-matched *db/db* mice. Of the 12 WD-fed mice, 33% exhibited mild (one inflammatory focus/1mm^2) and 66% had no observable inflammation. These numbers of WD-fed WT generally resembled that of *db/db* mice with, ~36% exhibiting various degrees of inflammatory foci/1mm^2 balanced by ~64% without any visual signs of hepatic inflammation (Figure 1N-O, 1X-Y).

Together, these findings demonstrate that genetic T2D does not recapitulate the severe, inflammatory liver disease triggered by a diet-induced model mimicking an unhealthy human diet, even under equivalent body weight, liver fat, and ALT elevations. They further show that hepatic cholesterol load alone is insufficient to drive liver inflammation, and that diet-derived metabolic stress – rather than hyperglycemia or T2D predisposition – is the primary driver of MASH.

Sixteen Weeks of FFMD Feeding Define a Critical Window for Cardiometabolic Intervention

Having established that the FFMD induces high-penetrance MASH and prediabetic (*db/db*)-like glucoregulatory disturbances, we next asked **when** the major cardiometabolic and hepatic pathologies supervene - and whether a discrete window exists in which disease trajectories diverge. Building on the robust liver pathology observed in C57BL/6J mice at T22 (Figure 1), we profiled FFMD-fed C57BL/6NTac mice from 4 to 24 weeks (Figure S2A), a substrain recently proposed as optimal for DIO-MASH studies when housed at thermoneutrality[4].

FFMD-fed mice developed **progressive insulin resistance and escalating hyperinsulinemia** with a close to 20-fold increase in peak GSIS response between week 4 and week 24, mirrored by a ~4-fold increase in liver weight (Figure S2B-C). ALT levels remained low at week 4 but doubled at week 8. This early increase remained stable until week 16 followed by a pronounced spike at week 24 (Figure S2D). Liver histology corroborated this trajectory with inflammatory scores parallelling measured ALT levels (Figure S2E-G).

The **concurrent surge in ALT and histopathology between weeks 16 and 24** delineates a transition point at which FFMD-driven metabolic dysfunction consolidates into advanced liver injury. Given the close connection of chronically elevated ALT levels and increased risk of CVD[21], based on our findings, we consider **16 weeks** an optimal and mechanistically informative window for probing the drivers of

progressive cardiometabolic pathology, capturing the convergence of intensified insulin resistance, increasing hepatocellular injury, and accelerating histological deterioration.

Thermoneutrality Uncouples Glucoregulatory Function from Cardiohepatic Decline

To interrogate the interrelationship between the cardiometabolic disease triad of interest, we continued our investigations in dyslipidemic male IGFII mice, prone to develop early T2D and CVD[14]. Utilizing ambient temperature as an experimental tool, we converged the above-described setups and housed our IGFII mice at either T22 or T30 to potentiate inflammation and fed them the MASH-inducing FFMD, or LFD reference, for either 16 or 24 weeks (Figure 2A). In the first 16-week cohort, mice housed at T22 were resistant to diet-induced obesity (Figure S3A-B), aligning with previous reports of this dyslipidemic mouse strain[14]. In contrast, their T30 housed counterparts close to doubled their weight gain within the first 16 weeks (Figure S3A). The reason behind this temperature-sensitive weight trajectory remains elusive and is highly debated in the field with inconsistent results across studies[10,11,22]. Peculiarly, our second cohort, where male mice were fed the obesogenic diet for 24 weeks, exhibited a different trait. Here, temperature-associated weight discrepancies were abolished (Figure S3C-D), enabling us to decouple temperature-associated cardiometabolic phenotypes from diet-induced obesity. We argue that despite the observed weight discrepancies between T22 housed mice from our first and second cohort, these results still substantiated 16 weeks of feeding as a window of opportunity for cardiometabolic interrogation.

Glucoregulatory assessment revealed stark temperature-dependent diabetic trajectories closely linked to feeding duration, but not body weight per se (Figure 2B-C, S3E-F). After 16 weeks, despite notable differences in body weight, all groups cleared their blood glucose after an oGTT (Figure 2B, S3E). However, after 24 weeks of feeding, in a cohort virtually matched on body weight (Figure S3C), ambient temperature served as the main driver of frank diabetes. Here, T22 housed mice – irrespective of diet – cleared their blood glucose, whereas T30 housed mice peaked later post-glucose challenge and failed to return to baseline (Figure 2C, S3F), indicative of early diabetes and increased risk of future CVD and all-cause mortality[23]. It is worth noting that, independently of body weight differences and time point, FFMD-fed mice housed at T22 exhibited modestly elevated fasting blood glucose levels (Figure S3E-F) but retained glucoregulatory clearance capacity. This aligns well with the concept that thermoneutrality unmasks latent diabetic phenotypes[24] by removing cold-induced sympathetic drive.

Next, we examined the hepatic disease burden of these dyslipidemic male cohorts. In our 16-week study, plasma lipid species and hepatic TAG, but not cholesterol, were highly elevated in mice housed at T30 (Figure 2D, S3G). However, in our second cohort with temperature groups not discordant for obesity, circulating and hepatic lipid burden were elevated solely as a function of diet (Figure 2D, S3H). Thus, after removing obesity as a confounder, ambient temperature appears to have little influence on lipid dynamics. Still, circulating ALT levels indicated more severe liver disease in mice housed at T30, irrespective of differences in body weight (Figure 2E). Histopathological assessment confirmed this trait

(Figure S3I-L), where I**nflammation (Figure 2F), fibrosis (Figure 2G-H), and cirrhosis penetrance (Figure S3M-O) were dictated by ambient temperature**.

Since IGFII mice are inherently prone to CVD, and the observed glucoregulatory phenotype intensifies human CVD risk, we next quantified aortic mineralization using high-resolution micro-computed tomography (μCT). Each sample generated ~1,000 z-stacked images at 14 μm thickness, enabling reconstruction of full three-dimensional mineralization volumes[25]. At 16 weeks - the inflection point linked to metabolic and hepatic phenotypic shifts - male mice had no mineralizations despite discordant obesity and ambient temperature status (Figure 2I). However, by 24 weeks, male **IGFII mice displayed a pronounced temperature-dependent** phenotype where all T30-housed, FFMD-fed mice presented with emerging **aortic mineralization contrasting only a single T20-housed mouse** (Figure 2I & S3P). As body weight developed similarly across temperatures, these data suggests that either glucoregulatory capacity (i.e., T2D) or MASH severity, rather than obesity *per se*, drives CVD risk.

To better dissect the hierarchy between these interrelated disease trajectories and in a sex-aware manner, we repeated the 24 week setup in female mice, known to present less glucoregulatory disturbances than males[26,27]. Independent of temperature, female IGFII mice fed FFMD gained **100% increase in baseline body weight** over 24 weeks (Figure S4A-B). While replicating the metabolic context of male mice in which body weight could be removed as a confounder, notable sex differences emerged, as expected, for the regulation of glucose homeostasis. Indeed, while FFMD feeding impaired the immediate glucose handling (Figure 2K), all female mice preserved glucoregulatory capacity and returned to baseline 2-h post challenge (Figure 2K- S4C). Still, T30 housed mice peaked later than their T22 housed counterparts, who instead presented mildly elevated fasting BG (Figure 2K-L); hence largely recapitulating the temperature-dependent pattern observed in male mice. Despite these temperature-dependent features, **female IGFII mice generally retained glycemic control**, thus enabling us to dissociate weight differences and glucoregulatory impairment from downstream cardiometabolic outcomes.

We next evaluated liver pathology and CVD burden. At first glance, FFMD-fed female IGFII mice exhibited a milder pathology, largely mirroring the 16-week male cohort in both magnitude and temperature profile for plasma and hepatic lipid species (Figure 2M-N, S4D-E), circulating ALT (Figure 2O), and liver inflammation (Figure 2P), as also evident from the histological grading of steatosis and MASH penetrance (Figure S4F-G). Ultimately advocating delayed disease progression**, female IGFII mice developed temperature-dependent cirrhosis (Figure 2Q-R, S4H-I) and aortic mineralization (Figure 2S & S4J), with a penetrance akin to that of 24 weeks FFMD-fed male IGFII mice on both parameters (Figure 2I, S3N-O). Thus, despite an apparently delayed hepatic inflammatory tone in female mice, the key cardiohepatic features of the male phenotype were fully reproducible across sexes**.

Ambient Temperature Mechanistically Dictate Diet-Induced Cardiohepatic Disease

Having established that thermoneutrality uncouples glucoregulatory control from progressive cardiohepatic injury, we next asked whether ambient temperature directly drive these diet-induced pathologies. To answer this, we designed a controlled temperature crossover study in female IGFII mice that minimizes confounding aspects of body weight and glucoregulatory status (Figure 3A). After 16 weeks of FFMD feeding at either T22 or T30, mice were either maintained at their initial condition or switched to the alternative temperature for a further eight weeks (Figure 3A). All groups were weight- and glycemia-matched immediately before the intervention, ensuring that subsequent differences reflected temperature-dependent trajectories rather than baseline metabolic burden.

Acute changes in temperature produced immediate, yet temporal, shifts in energy balance associated with an altered thermogenic demand[22,28] (Figure 3B-E). Transferring mice from T30 to T22 blunted weight gain, whereas switching from T22 to T30 released animals from cold-induced metabolic restraints and transiently increased weight gain (Figure 3B). As such, we observed a small tendency of mice swapped to an elevated ambient temperature gaining more weight post swap than their T22-housed maintained counterparts (Figure 3C). Similarly, mice moved from a warmer to a colder ambient temperature showed clear stagnation in weight gain following temperature swap (Figure 3C). Still, these short-term effects reflect the physiological adjustments to altered thermoregulatory demands and not long-term changes in disease trajectory. Indeed, terminal body weights ultimately converged across all FFMD-fed groups (Figure 3D). Consistent with established thermoregulatory physiology[29], food intake increased in cages swapped from T30 to T22, and decreased in cages moved from T30 to T22 (Figure 3E), essentially precluding altered energy intake as driver of the observed weight dynamics. Despite concluding the experiment at similar body weights, glucose tolerance was, as in the previous cohort, affected by ambient temperature (Figure 3F-H). To this end, T30-housed mice presented delayed glucose peak and increased fasting insulinemia compared to their T22-housed counterparts (Figure 3F, 3H). Swapping from T30 to T22 similarly improved glucose clearance (AUC, Figure 3F). Thus, although female IGFII mice generally retain their glucoregulatory capacity, T30-housing induce a response curve closely associated with clinical CVD risk[23].

We next dissected the effect on cardiac pathology (Figure 4A), which strongly supported the above notion. While **diet affected disease penetrance**, housing temperature dictated disease severity. This was qualitatively evident from aortas of mice after *en face* lipid staining (Figure 4B), and quantifiably by µCT assessment of aortic mineralization (Figure 4C & S4K). Importantly, temperature transitions tweaked the *magnitude*, but not the *presence*, of aortic mineralization burden. Thus, mice moved from T22 to T30 exhibited higher degree of detectable mineralization, whereas transitioning T30-housed mice to T22 reduced burden, likely reflecting changes in phenotype suppression rather than biological regression. Echocardiography further revealed that T30 conditions aggravated FFMD-induced cardiac dysfunction, including increased left ventricular hypertrophy, reduced ejection fraction, and fractional shortening (Figure 4D-F, Table S2). Taken together, these findings indicate that while cardiac pathology is primarily driven by diet, it is more pronounced during thermoneutral housing and closely associate with delayed glucose response curves.

Because T30 housing intensified the *detectability* of liver pathology (Figure 2), we next asked whether the crossover design would clarify the temperature-sensitivity of fibrosis. While plasma ALT levels showed a diet effect and suggested a uniform hepatic disease phenotype across ambient temperatures (Figure 2O, 4G), histological assessment revealed a more nuanced reality with notable temperature-dependencies on end-stage liver disease. Mice housed at T30 displayed higher fibrosis scores, greater fibrotic area, and a higher incidence of cirrhosis than those housed at T22 (Figure 4H-K). Importantly, switching temperatures shifted these readouts in a reciprocal manner: raising ambient temperature after 16 weeks increased detectable fibrosis and cirrhosis, whereas lowering temperature reduced them. This produced a near-linear relationship between cumulative weeks at T30, and the proportion of mice classified with cirrhosis (Figure 4J). No cirrhosis occurred in LFD-fed IGFII mice, confirming that the **obesogenic diet, rather than the dyslipidemic phenotype of these mice, is indispensable for the observed liver pathology**, while ambient temperature modulates its severity.

Thus, temperature manipulation serves as a powerful environmental driver to expose disease states that remain masked under conventional T22 housing conditions.

Ambient Temperature Unmasks Detrimental Hepatic Proteome Programs in Diet-Induced Liver Disease

To gain mechanistic insight into how FFMD feeding reshapes liver biology under different housing temperatures, we performed deep quantitative proteomics profiling of >6000 hepatic proteins, first in IGFII male mice (Figure 5A). The most variable proteins showed distinct clusters related to experimental variables such as diet, experimental duration, and degree of inflammation and fibrosis. The top 50 variable proteins were broadly proteins involved in immune activation, cellular architecture, vesicle trafficking, and DNA repair (Figure 5B), underscoring the broad remodeling of hepatic biology under FFMD challenge. While experimental duration was the main driver of data variation, experimental variables such as ambient temperature clearly separated proteomic states in the dyslipidemic male mice, virtually overlapping with inflammatory counts (Figure 5C-D).

Differential abundance and Gene Ontology (GO) enrichment analysis showed that FFMD feeding - regardless of housing temperature - strongly upregulated immune- and fibrosis-associated proteins (Lgals3, H2-Eb1, Gpnmb, Mpeg1) and biological processes linked to antimicrobial defense, extracellular matrix remodeling, and supramolecular fiber organization (Figure 5E-J). These signatures point toward programs involved in microbial translocation and fibrotic progression, aligning with suggested drivers of MASLD progression[30,31]. Notably, comparisons between T22- and T30-housed males revealed an additional layer of proteomic programs at T30, including tumorigenic, inflammatory, and angiogenic GO terms, accompanied by increased abundance of Ogn, Hbp1, Adgre1, and Elane (Figure 5I-J). These features suggest that T30 housing **release** tumor-associated hepatic programs that may be partially supressed by cold-induced metabolic stress at T22.

To test whether these temperature-associated signatures were the consequence of the more severe T2D-CVD-MASH triad observed in male mice - or whether they emerge independently of diabetes - we next turned to our female crossover cohort (Figure 6A). Because female IGFII mice retained glycemic

control and a generally lower body weight yet nevertheless developed severe cardiohepatic diseases, they provide an opportunity to disentangle the contribution of diabetes from the proteomic landscape. As in males, principal drivers of proteomic variance in females aligned with experimental variables such as housing temperature (Figure 6B), broadly mirroring the inflammatory tone of the livers (Figure 6C). Even in the absence of T2D, thermoneutrality increased the abundance of immune and fibrotic proteins (including Lgals3, Lpcat2, Gpnmb, Cd74, and Col14a1) (Figure 6D-I). Despite similar histological appearance for inflammation, the more sensitive proteomic readouts revealed enhanced inflammatory and fibrotic processes in T30-housed females. These data point toward a sex-, weight-, and glycemia-independent hepatic response to FFMD that is unmasked when thermal stress is removed.

Across both sexes, FFMD-feeding reproducibly enriched proteins involved in immune surveillance and extracellular matrix remodeling, along with biological processes related to cell migration, fibrosis, and defense against invading microorganisms (Figures 5 and 6). This convergence suggests a robust, diet-driven microbial translocation-inflammation axis, with ambient temperature modulating the detectability ad amplitude of these programmes rather than their presence.

Temperature shifts also reshaped broader proteome organisation in ways consistent with altered disease stage. In female mice, T30 selectively enriched terms related to extracellular matrix deposition and cell–matrix interactions, whereas increasing ambient temperature after 16 weeks revealed pathways involved in DNA repair, recombination and cell division (Figure 6J). Conversely, lowering temperature favoured metabolic and catabolic processes.

Together, these patterns support a model in which diet is the primary driver of hepatic immune, fibrotic and malignant remodelling, whereas ambient temperature acts as a physiological lens that exposes latent disease programmes without fundamentally changing their diet-driven origin.

Discussion

Here, we describe a preclinical model of MASLD/MASH that overcomes key translational barriers of current DIO-based rodent models. By incorporating human dietary patterns and housing mice at thermoneutrality, our model rapidly and robustly induces high-penetrance MASH without genetic modification or chemical inducers. The FFMD diet emerges as a powerful trigger of early, severe metabolic and hepatic disease in WT rodents within 12 weeks, and of pronounced cardiovascular and fibrotic comorbidities in dyslipidemic mice within 24 weeks. Thus, the DIO-MASH model presented here provides a versatile platform for mechanistic studies and therapeutic testing in cardiometabolic diseases.

Our findings demonstrate that diet composition – rather than caloric excess alone - is a major driver of hepatic pathology. Despite similar caloric content and macronutrient ratios, the FFMD induced substantially aggravated liver disease compared to WD, including higher degrees of inflammation, hypertrophy, and fibrosis. Traditionally WDs often employ supraphysical cholesterol and an overly simplified macronutrient composition with single sources of protein (casein), fat (lard) and carbohydrate

(fructose due to its stimulation of hepatic *de novo* lipogenesis[32]), which only partly reflect human dietary patterns. In contrast, the FFMD mimics fast-food consumption, combining a complex protein source, atherogenic fats, and soft drink-relevant sugar profiles, and thereby outperforms traditional WDs in provoking MASH. Whether this enhanced potency is primarily attributed to the mixed protein source, fat quality or sugar composition remains to be determined, but our data underlines the importance of macronutrient source and structure when modelling human MASH.

The MetS pandemic is characterized by an overconsumption of energy-dense foods, sugar-sweetened beverages and sedentary lifestyle - all risk factors for T2D and MASLD[33]. Consequently, the strong epidemiological association between T2D, MASLD, and CVD[3] may partially reflect shared upstream risk factors rather than strict causal dependencies. MASLD also develops in lean individuals[34], indicating that MASLD is not fully dependent on the obese state *per se*, but they share common risk factors. Recent large cohort studies of more than 13.000 individuals demonstrate that CVD and non-hepatocellular cancers are major causes of death in MASLD populations[35], underscoring the need to define causal components within the MASLD-T2D-CVD triad. In this context, we show that MASH severity in FFMD-fed mice was not recapitulated in weight-matched diabetic *db/db* mice, despite greater adiposity and higher hepatic cholesterol in the latter. This dissociation between genetic diabetes and MASH suggests that hepatic inflammation in our model is not solely driven by glucoregulatory impairment.

Furthermore, we demonstrate that ambient temperature is a critical determinant of disease trajectory in preclinical cardiometabolic research. Mice housed at T30 developed markedly worse liver pathology, insulin resistance, and cardiovascular disease than those housed at T22, despite consuming less food. These findings are consistent with previous work showing that thermoneutral housing unmasks a protective mechanism by eliminating adaptive thermogenesis, thus better aligning murine metabolism to that of humans[36]. Here, T30 not only accelerated weight gain and insulin resistance, but also markedly exacerbated fibrosis, cirrhosis, aortic mineralization, and cardiac abnormalities. Importantly, switching animals from T30 to T22 attenuated these features, whereas increasing ambient temperature after 16 weeks intensified them, indicating that temperature acts as a tunable environmental variable that can modify cardiometabolic disease trajectories. This has practical implications for drug development, where adjusting housing temperature may allow investigators to model distinct stages of cardiometabolic disease and probe treatment efficacy under more human-relevant conditions.

Sex differences emerged as an additional variable in modulating the MASLD-T2D-CVD relationship. Dyslipidemic mice of both sexes developed end-stage liver disease and CVD under FFMD and T30 conditions, but only male mice progressed to frank T2D, despite comparable weight gain and adiposity. This pattern mirrors human epidemiology in which men typically develop T2D at lower BMI, younger age, and with higher incidence than women[37,38]. Notably, female IGFII mice remained largely protected from T2D yet still developed significant inflammation, fibrosis, cirrhosis, and aortic mineralization under thermoneutral FFMD feeding. Together with our cross-over design, these findings indicate that the effects observed at T30 are not secondary to differences in food intake or body weight but reflect

temperature-dependent unmasking of latent cardiohepatic programmes. They further support the notion that T2D can contribute to but is not a prerequisite for progressive MASLD or CVD, and that sex-specific factors modulate how shared metabolic stressors translate into organ-specific pathology.

Deep hepatic proteomics provided mechanistic support for a profoundly diet-dependent but temperature-modulated model of disease progression. Across sexes and temperatures, FFMD feeding reproducibly enriched proteins involved in immune surveillance, extracellular matrix remodelling and defence against microbial stimuli, aligning with proposed roles of microbial translocation and immune activation in MASLD progression[30,33,39]. Temperature shifts dynamically altered these programmes, with T30 promoting angiogenesis and DNA repair pathways - hallmarks of tumorigenesis – particular in male mice. In contrast, female mice showed temperature-sensitive changes in DNA repair and cell-cycle pathways on a background of preserved glycaemic control, suggesting that T2D is not required for activation of these programmes but may accelerate or magnify them, particularly in males. These patterns, together with epidemiological links between hyperinsulinaemia and cancer mortality[40], raise the possibility that T2D acts as a tumour-promoting modifier rather than an essential driver of MASH itself. While it would have been of interest to explore if prolonged FFMD-feeding in female dyslipidemic mice would eventually result in deteriorated glucoregulatory capacity and tumorigenic processes, such exploration is hampered by the disease severity of the dyslipidemic IGFII model where several mice died spontaneously of strokes, most likely related to chronic FFMD-induced cardiohepatic oucomes. Overall, our proteomic data reinforce a central conclusion: diet is the primary driver of hepatic immune, fibrotic and tumour-associated remodelling, while ambient temperature functions as a physiological gauge, exerting a fine tuning of the full spectrum of cardiohepatic pathogenic programmes.

This study has several limitations. First, although we included both wild-type and dyslipidemic IGFII mice and analysed both sexes, our work is restricted to murine models and does not address inter-individual genetic variation at the level seen in humans. Second, our proteomic analyses are associative and do not causally dissect specific immune or tumourigenic pathways, or the contribution of bacterial translocation to the observed signatures. Finally, we focused on a single humanized diet formulation; whether similar temperature-dependent relationships hold across other dietary patterns remains to be tested. Future work integrating microbiome manipulations, gut barrier function, pathway-specific interventions, and pharmacological testing at defined disease stages will be important to fully exploit this platform for translational purposes.

Taken together, our work establishes the use of our FFMD diet as a fully penetrant, yet modifiable and human-relevant tool for preclinical modelling of human MASH and related cardiovascular complications. When combined with thermoneutral housing and genetically dyslipidemic mice, it enables rapid, reproducible induction of the full spectrum of MetS - including obesity, T2D, MASH and liver cirrhosis, atherosclerosis and aortic mineralization - all within a 16-24-week window. This model avoids chemical inducers or aging-based confounders, increases clinical relevance, and captures the complex interplay between diet, environment, and sex in cardiometabolic disease pathogenesis. As such, it represents a

valuable framework for investigating mechanisms of disease and for testing emerging therapeutic agents targeting MASLD and its comorbidities.

Materials and Methods

Study approval and ethics

All animal experiments were approved by the Canadian Council on Animal Care under Laval University license (#2017-086) and the Danish Animal Inspectorate (#2021-15-0201-01031), and were conducted in accordance with national guidelines.

Mice housing and experimental design:

Male C57BL/6J and C57BL/6NTac mice were obtained from Jackson Laboratory and Taconic, respectively, and housed in specific pathogen-free facilities on a 12 h light–dark cycle with ad libitum access to food and water. Dyslipidaemic LDLr−/−/ApoB100/100/IGF-II (IGFII) mice on a C57BL/6 background were bred in-house[13]. Upon arrival or weaning, mice were acclimatized for 10–14 days on a low-fat control diet and their respective housing temperature before randomisation to experimental groups matched for baseline body weight and body composition. Mice were housed three per cage in all experiments.

Ambient temperature was maintained at either standard room temperature (T22, ~20–22 °C) or thermoneutrality (T30, ~28–30 °C) in dedicated climate-controlled cabinets. For crossover experiments, mice were transferred between T22 and T30 rooms at the designated time point. All tests were performed at the temperature at which the mice were housed in dedicated procedure rooms.

Bodyweight was recorded weekly and food intake three times per week. Body composition (fat and lean mass) was assessed by quantitative magnetic resonance (EchoMRI or Minispec LF290 NMR, Bruker) at baseline and at indicated time points.

Wild-type C57BL/6J diet-comparison cohort

Male C57BL/6J mice (8 weeks old) were fed for 12 weeks with either a humanized fast food-mimicking diet (FFMD), a Western diet (WD) matched for total energy and macronutrient distribution, or a compositionally defined low-fat diet (LFD) used as eucaloric reference (Ssniff Spezialdiäten; Table S1). All mice were housed at T22.

db/db cohort

Male leptin receptor-deficient db/db mice and db/+ controls (Jackson Laboratory) were maintained on standard chow from 8 to 18 weeks of age and housed at T22. These mice served as a genetic T2D reference group and were studied in parallel with FFMD-fed C57BL/6J mice matched for body weight and liver fat.

C57BL/6NTac time-course cohort

Male C57BL/6NTac mice were fed FFMD from 8 weeks of age and sacrificed after 4, 8, 16, or 24 weeks of feeding to define temporal inflection points for metabolic and hepatic pathology (Figure S2).

IGFII male and female cohorts

Male and female IGFII mice were fed FFMD or LFD from 8 to 32 weeks of age under either T22 or T30 conditions (Figure 2A). Cohorts were designed to evaluate temperature-dependent trajectories of obesity, glucoregulatory control, liver disease and cardiovascular pathology. A 16-week male cohort was used to define early disease stages; a 24-week male cohort and a 24-week female cohort were used to study advanced disease and sex differences.

Temperature crossover cohort

To directly test the causal impact of ambient temperature on disease progression, female IGFII mice were fed FFMD at either T22 or T30 for 16 weeks, then either maintained at their initial temperature or switched to the alternative temperature for an additional 8 weeks (Figure 3A). All four groups were matched for body weight and glycaemia at week 16.

Diets

Experimental diets were produced by Ssniff Spezialdiäten (Germany). The LFD (catalogue number S9552-E026) was a compositionally defined low-fat diet matched in protein sources to the FFMD. The FFMD (D12079 mod.) was designed to mimic human fast-food patterns, with mixed protein sources (casein, poultry, soy, egg), atherogenic fats (butter fat, lard, vegetable oils), physiologically relevant cholesterol, and a carbohydrate fraction enriched in sucrose and fructose at a ratio resembling sugar-sweetened beverages (catalogue number S9552-E024). The WD was a commonly used high-fat, high-sucrose diet (45 kcal% fat) with simplified macronutrient sources and comparable total energy density (D12451). Energy content and macronutrient distribution were provided by the manufacturer and are summarized in Table S1. Fresh diet was provided three times per week and intake measured per cage.

Oral Glucose Tolerance Tests and Insulin Secretion Assay

Oral glucose tolerance tests (oGTTs) were performed after a 5h morning fast (starting 2 h into the light phase) or 12h hour overnight fast (db/db mice only) as indicated in figure legends. Baseline (time 0) blood glucose was measured from the tail vein using a handheld glucometer (e.g., OneTouch Verio Flex, LifeScan). Mice then received an oral gavage of dextrose (1.0–1.5 g/kg lean mass; dose specified in figure legends) and blood glucose was measured at 15, 30, 60, 90 and 120 min.

Blood samples for plasma insulin were collected into EDTA-coated capillaries at baseline and selected time points, kept on ice, centrifuged at 1,000 × g for 10 min at 4 °C, and stored at −80 °C. Plasma insulin

was quantified using an ultrasensitive mouse insulin ELISA (Alpco) or mesoscale technology (MSD) according to the manufacturers' protocols.

Biochemical Analyses

Triacylglycerides in liver tissue were measured using an organic solvent extraction followed by enzymatic quantification by the Medical Laboratory of the Quebec Heart and Lung Institute by colorimetric analysis using the Siemens Dimension Vista® 1500 system. Briefly, snap-frozen liver samples stored at −80 °C were cryo-ground in liquid nitrogen, and approximately 50 mg tissue was transferred to tubes containing 0.9 mL chloroform:methanol (2:1, v/v) and stainless-steel beads, then homogenised for 1 min at 50 Hz using a TissueLyser LT (Qiagen). After addition of 0.3 mL methanol, samples were rotated for 2 h and centrifuged for 15 min at 4,000 × g at 10 °C. The resulting supernatant (0.825 mL) was transferred to fresh tubes, mixed with 0.4 mL chloroform, vortexed, followed by addition of 0.275 mL 0.73% NaCl, another brief vortex and centrifugation for 3 min at 4,000 × g at 10 °C to induce phase separation. The upper phase was discarded, and the organic phase was washed three times with 0.8 mL Folch solution (chloroform:methanol:0.58% NaCl, 3:48:47, v/v/v), adding a few drops of methanol until the solution became clear upon vortexing. Organic solvents were evaporated under a nitrogen stream, and the lipid residue was dissolved in isopropanol containing 10% Triton X-100. TAG content was then determined using the Infinity Triglycerides Reagent (Thermo Fisher Scientific) against serially diluted standards.

Liver Histology

Liver tissue from the right medial lobe (lobus dexter medialis hepatis) was collected and fixed in 4% paraformaldehyde for 3 days. Samples were paraffin-embedded, sectioned at 3 µm, and stained with hematoxylin and eosin (H&E) or Sirius Red. Histological assessment was performed blinded to experimental groups by one to three experienced pathologists. MASLD activity was evaluated in H&E-stained sections using an established scoring system for murine MASLD as previously described[16]. Briefly, hepatocellular hypertrophy as well as macrovesicular and microvesicular steatosis were assessed at 40x-100x magnification and quantified relative to the total liver area. Hepatic inflammation was determined by counting inflammatory foci per mm² at 100× magnification, defining a focus as a cluster (rather than a row) of at least five inflammatory cells, and averaging counts from five random fields. Fibrosis was graded blindly on Sirius Red–stained sections according to the Ishak staging system, which sensitively integrates both extent and anatomical distribution of fibrosis. Cirrhosis was defined as Ishak stage 5–6[20].

Echocardiography, µCT, and *en face*

Echocardiographic images were obtained blinded operators using a Vevo 3100 imaging system (VisualSonics, FUJIFILM, Toronto, Canada) equipped with a 40-MHz transducer (MX550S), as previously described[41]. Anesthesia was induced in a dedicated chamber using 4-5% isoflurane. Mice were then positioned in a supine position on a heated platform, and anesthesia was maintained via a nose

delivering 1.5-3% isoflurane. Fur from the thoracic and abdominal regions was removed using a depilatory cream prior to imaging. Briefly, echocardiographic images were obtained from the left ventricular parasternal long-axis (PSLAX; B-mode and M-mode) view. PSLAX images were used to trace the left ventricle at end-diastole and end-systole. These tracings were then used to calculate averaged values for end-diastolic volume, end-systolic volume, and ejection fraction (EF). Internal LV diameters at end-diastole (LVIDd) and end-systole (LVIDs), were measured from PSLAX M-mode recordings to provide linear dimensions of left ventricular function, calculated as fractional shortening (FS). All calculations were made using VevoLab software (VisualSonics).

After Echocardioography, mice were dissected and aortic roots were prepared and scanned ex vivo to quantify mineralised lesions by high-resolution micro-computed tomography (μCT). After dissection, hearts and proximal aortas were briefly blotted and immersed for ~10 min in an iopamidol-based contrast solution (Niopam 300 contrast agent diluted 1:4 in Milli-Q water) to enhance soft-tissue contrast, ensuring that the entire aortic root and valve region were submerged. Immediately before scanning, samples were perfused via the aortic arch with corn oil using a blunted 27G needle to displace residual buffer and contrast, taking care to fill the aortic root and valve region completely and to avoid air bubbles, and then transferred to 1.5 mL tubes prefilled with corn oil and positioned with the heart downward and the ascending aorta upright. Scanning was performed on a Skyscan 1174 system (Bruker) operated at 50 kV and 403 μA, without filter, yielding an isotropic voxel size of ~13.7–14 μm (~1,000 z-stacks per sample). Projection images were reconstructed using NRecon (Bruker) with smoothing set to 4, ring artefact reduction of 6, beam-hardening correction of 25%, and a reconstruction range of 0–0.15. Regions of interest encompassing the aortic valve leaflets and adjacent outflow tract were defined, and mineralized tissue was segmented in CTan (Bruker) using a fixed global intensity threshold applied uniformly across samples, as previously described for vascular mineralization analyses[25]. Mineralization burden was expressed as total calcified volume within the aortic region in three dimensions, and a mineralization score was curated where a volume less than 0.001μm^3 gave a score of 0, between 0.001-0.05μm^3 gave a score of 1, between 0.05 and 0.1μm^3 gave a score of 2, and anything above 0.1μm^3 scored 3. After μCT scan atheroma lesions were quantified according to the *en face* technique[42]. Briefly, excised aortas were stored under 4 °C in 5% formalin. Perivascular adipose tissue was removed, and the aorta was bisected exposing the intima layer. The aorta was then pinned *en face* and stained with 0.5% Sudan IV. Images were captured using a camera attached to a Leica MZ6 dissecting microscope.

Liver Proteomics

Liver proteomics was performed with detailed experimental procedures including sample preparation, LC gradients, acquisition parameters, data processing settings, and acquisition parameters for the Q Exactive HF-X as described in detail elsewhere[43,44]. Briefly, for quantitative proteomics, liver samples were processed using a protein aggregation capture workflow followed by LysC/trypsin digestion, C18 StageTip desalting, and LC-MS/MS analysis in data-independent acquisition mode. Peptides were

separated on an EASY-nLC 1000 coupled to a Q Exactive HF-X or Orbitrap Exploris 480 mass spectrometer and analyzed using Spectronaut (v16) with an in-house spectral library.

Quantitative proteomic data were preprocessed using the DEP R package framework[45], including log2 transformation, variance stabilizing normalization[46], and missing value imputation based on the nature of missingness. Proteins missing in all replicates of at least one condition were classified as missing not at random (MNAR) and imputed by random draws from a Gaussian distribution centered at a minimal value[46]. Remaining values were considered missing at random (MAR) and imputed using the k-nearest neighbor algorithm. DEP, which utilizes functions from MSnbase, was applied with default parameters[47,48].

Statistical Analyses

Statistical analyses were performed using GraphPad Prism (version 10; GraphPad Prism). Data are presented as mean ± SEM, with individual values displayed to illustrate data distribution, unless otherwise indicated in the corresponding figure legends. For experiments including more than two groups with one independent variable, statistical evaluation was conducted using one-way ANOVA followed by Tukey's multiple comparisons test. Comparisons between two groups were analyzed using two-tailed unpaired Student's t-tests. A p value < 0.05 was considered statistically significant. Sample sizes were not determined using a priori power calculations, and no data points were excluded from the analyses. Upon arrival, animals were allocated to experimental groups after matching for baseline body weight and body composition. Differential protein abundance was assessed using Welch's ANOVA implemented in the stats R package (v4.2.1), followed by Benjamini–Hochberg correction for multiple testing. Post hoc comparisons were performed using the Tukey honestly significant difference (HSD) test[49]. Proteins were deemed significantly different with a q-value ≤ 0.05 (for both ANOVA and post hoc tests) and $|\log2\,FC| \geq 1$. Volcano plots were generated using ggplot2 (v3.4.0). Principal component analysis (PCA) was conducted via the stats package and visualized using the ggplot2 *autoplot* function. Gene set enrichment analysis (GSEA) was performed with ClusterProfiler (v4.6.0)[50] against the Gene Ontology database[51,52], and enrichment significance was defined at $q \leq 0.25$ after Benjamini–Hochberg correction.

Declarations

Data availability

The mass spectrometry proteomics data have been deposited to the ProteomeXchange Consortium via the PRIDE[53] partner repository with the project accession number PXD075482 (**Reviewer account details** for the review phase only, link will be made publicly available and non-password restricted at publication: Username: reviewer_pxd075482@ebi.ac.uk, Password: E3r1xcKgrcFR). All datasets included in the current study are available in the Figshare repository DOI: 10.6084/m9.figshare.31494070 or from the

corresponding author upon request. (**Reviewer link during the** review phase only, link will be made publicly available at publication: https://figshare.com/s/681a26c12c998b867dc2)

Acknowledgements:

This study was mainly supported by Novo Nordisk Foundation grant (NNF17OC0026698; NNF21OC006693) issued to B.A.H.J., and by a CIHR Foundation Scheme grant issued to A.M (FDN-143247). A.M. was supported by a CIHR/Pfizer research Chair in the pathogenesis of insulin resistance and cardiovascular diseases and B.A.H.J. was further supported by a Lundbeck Fellowship grant (R232-2016-2425). Figure cartoons were adapted CC0 content available from Bioicons.com. We thank Annette Schumacher (Ssniff Spezialdiäten) for valuable input on diet design and assistance with diet formulation. We also thank Joanie Dupont-Morissette, Christine Dallaire, Jacinthe Julien, Marie-Josée Beaulieu, Lia Perazza, and Renato Nachbar (Université Laval) for their excellent technical assistance.

Contributions:

Conceptualization: B.A.H.J., A.M., **Methodology:** B.A.H.J., A.M., **Diet Design:** B.A.H.J., **Investigation - In Vivo Analysis:** B.A.H.J., S.K.Y.J., L.R.P., I.S.L., M.A., L.D., V.V., **Investigation - Echocardiography (data acquisition, analysis, interpretation):** L.R.P., **Investigation - Ex Vivo Analysis:** B.A.H.J., S.K.Y.J., T.S., B.F., V.V., L.K., P.H., I.S.L., M.A., P.B.P., L.D., P.M., **Investigation - Liver, Histology:** B.F., B.A.H.J., S.K.Y.J., J.C.B.J., **Investigation - Liver Proteomics:** T.S. (lead), S.K.Y.J. (support), under supervision of T.G., **Investigation - Genotyping:** M.A. (lead), **Data Integration:** B.A.H.J., S.K.Y.J., **Writing - Original Draft:** B.A.H.J., S.K.Y.J., **Writing - Review & Editing:** B.A.H.J., S.K.Y.J., P.L.M, A.M., **Supervision:** B.A.H.J., A.M, **Approval of Final Manuscript:** All authors.

Conflicts of Interest:

The authors declare no conflicts of interest.

References

1. Noubiap, J. J. *et al.* Geographic distribution of metabolic syndrome and its components in the general adult population: A meta-analysis of global data from 28 million individuals. *Diabetes Res. Clin. Pract.* **188**, 109924 (2022).
2. Neeland, I. J. *et al.* Metabolic syndrome. *Nat. Rev. Dis. Prim.* **10**, 77 (2024).
3. Younossi, Z. M. *et al.* The Global Epidemiology of Nonalcoholic Fatty Liver Disease and Nonalcoholic Steatohepatitis Among Patients With Type 2 Diabetes. *Clin. Gastroenterol. Hepatol.* (2024) doi:https://doi.org/10.1016/j.cgh.2024.03.006.
4. Vacca, M. *et al.* An unbiased ranking of murine dietary models based on their proximity to human metabolic dysfunction-associated steatotic liver disease (MASLD). *Nat. Metab.* **6**, 1178–1196 (2024).

5. Gallage, S. *et al.* A researcher's guide to preclinical mouse NASH models. *Nat. Metab.* **4**, 1632–1649 (2022).
6. Neff, E. P. A point on thermoneutrality for mice . *Lab Anim. (NY).* **49**, 169 (2020).
7. Škop, V. *et al.* Mouse Thermoregulation: Introducing the Concept of the Thermoneutral Point. *Cell Rep.* **31**, 107501 (2020).
8. Clayton, Z. S. & McCurdy, C. E. Short-term thermoneutral housing alters glucose metabolism and markers of adipose tissue browning in response to a high-fat diet in lean mice. *Am. J. Physiol. Integr. Comp. Physiol.* **315**, R627–R637 (2018).
9. Fischer, A. W. *et al.* Optimal housing temperatures for mice to mimic the thermal environment of humans : An experimental study. *Mol. Metab.* (2018) doi:10.1016/j.molmet.2017.10.009.
10. Tian, X. Y. *et al.* Thermoneutral Housing Accelerates Metabolic Inflammation to Potentiate Atherosclerosis but Not Insulin Resistance. *Cell Metab.* **23**, 165–178 (2016).
11. Giles, D. A. *et al.* Thermoneutral housing exacerbates nonalcoholic fatty liver disease in mice and allows for sex-independent disease modeling. *Nat. Med.* **23**, 829–838 (2017).
12. Giles, D. A. *et al.* Modulation of ambient temperature promotes inflammation and initiates atherosclerosis in wild type C57BL/6 mice. *Mol. Metab.* **5**, 1121–1130 (2016).
13. Laplante, M.-A. *et al.* Distinct metabolic and vascular effects of dietary triglycerides and cholesterol in atherosclerotic and diabetic mouse models. *Am. J. Physiol. Metab.* **305**, E573–E584 (2013).
14. Le Quang, K. *et al.* Early Development of Calcific Aortic Valve Disease and Left Ventricular Hypertrophy in a Mouse Model of Combined Dyslipidemia and Type 2 Diabetes Mellitus. *Arterioscler. Thromb. Vasc. Biol.* **34**, 2283–2291 (2014).
15. Perazza, L. R. *et al.* Fish oil replacement prevents, while docosahexaenoic acid-derived protectin DX mitigates end-stage-renal-disease in atherosclerotic diabetic mice. *FASEB J.* **35**, e21559 (2021).
16. Larsen, I. S. *et al.* Experimental diets dictate the metabolic benefits of probiotics in obesity. *Gut Microbes* **15**, (2023).
17. Abid, A. *et al.* Soft drink consumption is associated with fatty liver disease independent of metabolic syndrome. *J. Hepatol.* **51**, 918–924 (2009).
18. Jensen, T. *et al.* Fructose and sugar: A major mediator of non-alcoholic fatty liver disease. *J. Hepatol.* **68**, 1063–1075 (2018).
19. Feingold, K. R., Lear, S. R. & Moser, A. H. De novo cholesterol synthesis in three different animal models of diabetes. *Diabetologia* **26**, 234–239 (1984).
20. Ishak, K. *et al.* Histological grading and staging of chronic hepatitis. *J. Hepatol.* **22**, 696–699 (1995).
21. Schindhelm, R. K. *et al.* Alanine aminotransferase predicts coronary heart disease events: A 10-year follow-up of the Hoorn Study. *Atherosclerosis* **191**, 391–396 (2007).
22. Choi, B. S.-Y. *et al.* Housing matters: Experimental variables shaping metabolism in obese mice. *Mol. Metab.* **98**, 102190 (2025).

23. Hulman, A. *et al.* Glucose patterns during an oral glucose tolerance test and associations with future diabetes, cardiovascular disease and all-cause mortality rate. *Diabetologia* **61**, 101–107 (2018).
24. Wang, X. *et al.* Delay in glucose peak time during the oral glucose tolerance test as an indicator of insulin resistance and insulin secretion in type 2 diabetes patients. *J. Diabetes Investig.* **9**, 1288–1295 (2018).
25. Huesa, C., Millán L., J., van 't Hof J., R. & MacRae E., V. A new method for the quantification of aortic mineralization by three-dimensional micro-computed tomography. *Int J Mol Med* **32**, 1047–1050 (2013).
26. Pettersson, U. S., Waldén, T. B., Carlsson, P.-O., Jansson, L. & Phillipson, M. Female Mice are Protected against High-Fat Diet Induced Metabolic Syndrome and Increase the Regulatory T Cell Population in Adipose Tissue. *PLoS One* **7**, e46057 (2012).
27. Maric, I. *et al.* Sex and Species Differences in the Development of Diet-Induced Obesity and Metabolic Disturbances in Rodents. *Front. Nutr.* **9**, (2022).
28. John, L. M. *et al.* Housing-temperature reveals energy intake counter-balances energy expenditure in normal-weight, but not diet-induced obese, male mice. *Commun. Biol.* **5**, 946 (2022).
29. Jacobsen, J. M. *et al.* Neither rats nor mice have a broad thermoneutral zone: implications for physiological studies. *Commun. Biol.* (2026) doi:10.1038/s42003-026-09534-w.
30. Simbrunner, B. *et al.* Bacterial translocation occurs early in cirrhosis and triggers a selective inflammatory response. *Hepatol. Int.* **17**, 1045–1056 (2023).
31. Männistö, V. *et al.* Serum lipopolysaccharides predict advanced liver disease in the general population. *JHEP Reports* **1**, 345–352 (2019).
32. Todoric, J. *et al.* Fructose stimulated de novo lipogenesis is promoted by inflammation. *Nat. Metab.* **2**, 1034–1045 (2020).
33. Tilg, H., Adolph, T. E., Dudek, M. & Knolle, P. Non-alcoholic fatty liver disease: the interplay between metabolism, microbes and immunity. *Nat. Metab.* **3**, 1596–1607 (2021).
34. Younes, R. *et al.* Caucasian lean subjects with non-alcoholic fatty liver disease share long-term prognosis of non-lean: time for reappraisal of BMI-driven approach? *Gut* **71**, 382 LP – 390 (2022).
35. Issa, G., Shang, Y., Strandberg, R., Hagström, H. & Wester, A. Cause-specific mortality in 13,099 patients with metabolic dysfunction-associated steatotic liver disease in Sweden. *J. Hepatol.* **83**, 643–651 (2025).
36. Fischer, A. W., Cannon, B. & Nedergaard, J. The answer to the question "What is the best housing temperature to translate mouse experiments to humans?" is: thermoneutrality. *Mol. Metab.* **26**, 1–3 (2019).
37. Kautzky-Willer, A., Leutner, M. & Harreiter, J. Correction to: Sex differences in type 2 diabetes. *Diabetologia* **66**, 1165 (2023).
38. Lamri, A. *et al.* Insight into genetic, biological, and environmental determinants of sexual-dimorphism in type 2 diabetes and glucose-related traits. *Front. Cardiovasc. Med.* **Volume 9-2022**,

(2022).
39. Krenkel, O. *et al.* Myeloid cells in liver and bone marrow acquire a functionally distinct inflammatory phenotype during obesity-related steatohepatitis. *Gut* **69**, 551 LP – 563 (2020).
40. Tsujimoto, T., Kajio, H. & Sugiyama, T. Association between hyperinsulinemia and increased risk of cancer death in nonobese and obese people: A population-based observational study. *Int. J. Cancer* **141**, 102–111 (2017).
41. Walsh-Wilkinson, É. *et al.* Age and sex hormones modulate left ventricle regional response to angiotensin II in male and female mice. *Am. J. Physiol. Circ. Physiol.* **323**, H643–H658 (2022).
42. Perazza, L. R. *et al.* Dietary sucrose induces metabolic inflammation and atherosclerotic cardiovascular diseases more than dietary fat in LDLr−/− ApoB100/100 mice. *Atherosclerosis* **304**, 9–21 (2020).
43. Bendixen, S. M. *et al.* Single cell-resolved study of advanced murine MASH reveals a homeostatic pericyte signaling module. *J. Hepatol.* **80**, 467–481 (2024).
44. Boel, F. *et al.* Deep proteome profiling of metabolic dysfunction-associated steatotic liver disease. *Commun. Med.* **5**, 56 (2025).
45. Zhang, X. *et al.* Proteome-wide identification of ubiquitin interactions using UbIA-MS. *Nat. Protoc.* **13**, 530–550 (2018).
46. Huber, W., von Heydebreck, A., Sültmann, H., Poustka, A. & Vingron, M. Variance stabilization applied to microarray data calibration and to the quantification of differential expression. *Bioinformatics* **18**, S96–S104 (2002).
47. Gatto, L., Gibb, S. & Rainer, J. MSnbase, Efficient and Elegant R-Based Processing and Visualization of Raw Mass Spectrometry Data. *J. Proteome Res.* **20**, 1063–1069 (2021).
48. Gatto, L. & Lilley, K. S. MSnbase-an R/Bioconductor package for isobaric tagged mass spectrometry data visualization, processing and quantitation. *Bioinformatics* **28**, 288–289 (2012).
49. Tukey, J. W. Comparing Individual Means in the Analysis of Variance. *Biometrics* **5**, 99–114 (1949).
50. Wu, T. *et al.* clusterProfiler 4.0: A universal enrichment tool for interpreting omics data. *Innov.* **2**, 100141 (2021).
51. Ashburner, M. *et al.* Gene Ontology: tool for the unification of biology. *Nat. Genet.* **25**, 25–29 (2000).
52. Consortium, T. G. O. The Gene Ontology resource: enriching a GOld mine. *Nucleic Acids Res.* **49**, D325–D334 (2021).
53. Perez-Riverol, Y. *et al.* The PRIDE database resources in 2022: a hub for mass spectrometry-based proteomics evidences. *Nucleic Acids Res.* **50**, D543–D552 (2022).

Figures

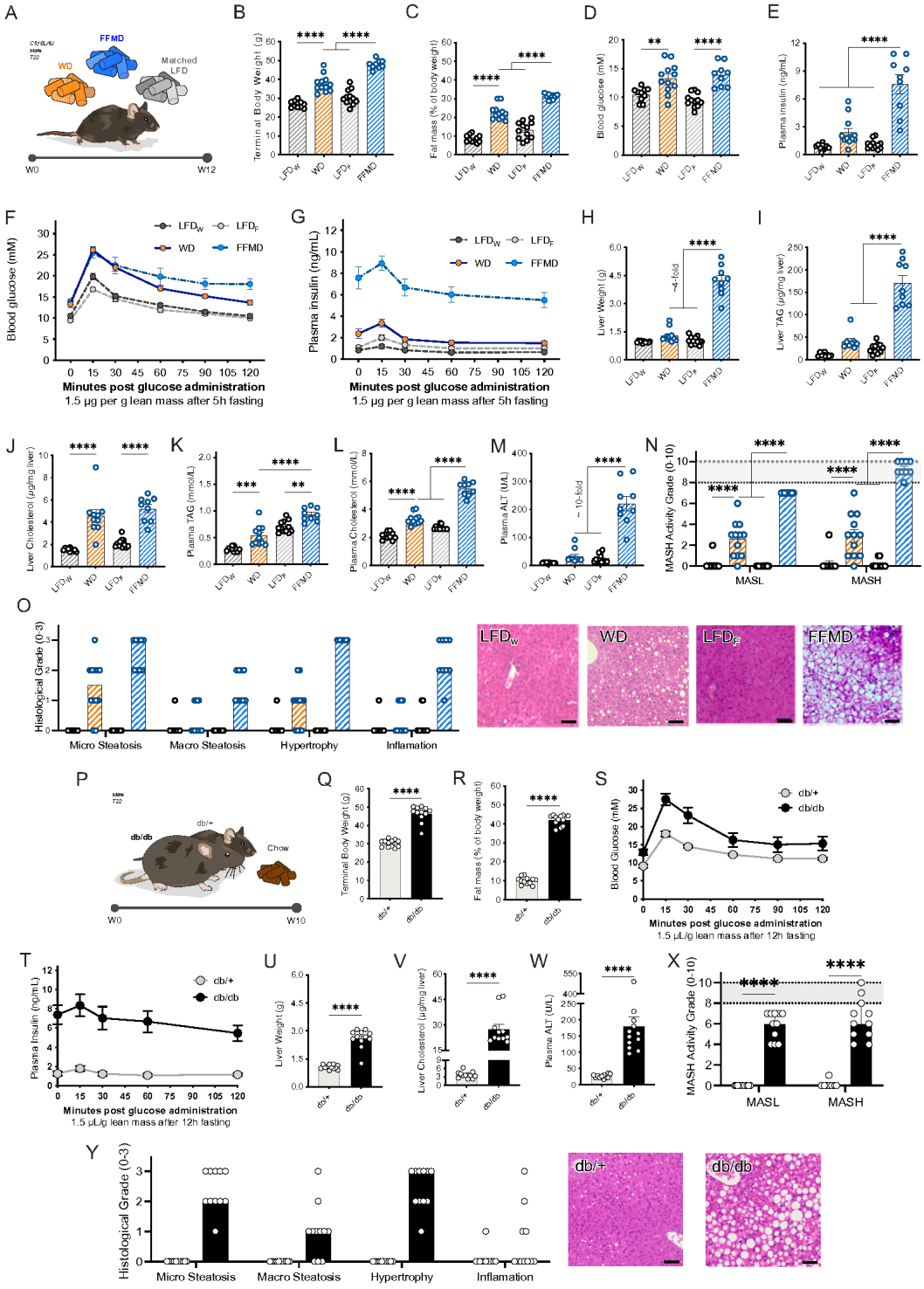


Figure 1

The Fast-food mimicking diet (FFMD) displays enhanced liver preference and liver disease independent of frank diabetes. (A) Study schematics of the wild-type diet comparison study. (B) Body weights of mice at termination, shown as the mean ± SEM. (C) Fat mass relative to body weight at termination, shown as the mean ± SEM. (D) Fasting blood glucose levels after a 5-hour fast, shown as the mean ± SEM. (E) Fasting insulin levels after a 5-hour fast, shown as the mean ± SEM. (F) Longitudinal blood glucose levels

after an oral glucose tolerance test (oGTT), shown as the mean ± SEM. (G) Longitudinal plasma insulin levels after an oGTT, shown as the mean ± SEM. (H) Liver wet weights, shown as the mean ± SEM. (I) Liver triacylglyceride (TAG) levels adjusted for tissue input, shown as the mean ± SEM. (J) Liver cholesterol levels adjusted for tissue input, shown as the mean ± SEM. (K) Plasma TAG levels, shown as the mean ± SEM. (L) Plasma cholesterol levels, shown as the mean ± SEM. (M) Plasma alanine aminotransferase (ALT) levels, shown as the mean ± SEM. (N) Combined histopathological MASH activity score based on steatosis, hypertrophy, and inflammation, shown as the mean ± SEM. A range of 8-10 (grey shaded area) indicates frank MASH. (O) Histological scores of steatosis types, hypertrophy, and inflammation, shown as the median, with representative histology pictures. (P) Study schematics of the db/db study. (Q) Body weights of db/db mice at termination, shown as the mean ± SEM. (R) Fat mass relative to body weight at termination, shown as the mean ± SEM. (S) Longitudinal blood glucose levels of db/db mice after an oGTT, shown as the mean ± SEM. (T) Longitudinal plasma insulin levels after an oGTT, shown as the mean ± SEM. (U) Wet weights of db/db livers, shown as the mean ± SEM. (V) Liver cholesterol levels, shown as the mean ± SEM. (W) Plasma ALT levels, shown as the mean ± SEM. (X) MASH Activity scores, shown as the mean ± SEM. (Y) Histological scores of steatosis types, hypertrophy, and inflammation, shown as the median, with representative histology pictures. Scale bars are 50 μm. N = 8-12 per group, with individual data points representing each mouse. When comparing more than two groups, data were analysed with a one-way ANOVA with Tukey's multiple comparison test, and when comparing two groups a two-tailed unpaired t-test was performed. Statistical significance was considered at $p < 0.05$, where * = $p < 0.05$, ** = $p < 0.01$, *** = $p < 0.001$, **** = $p < 0.0001$.

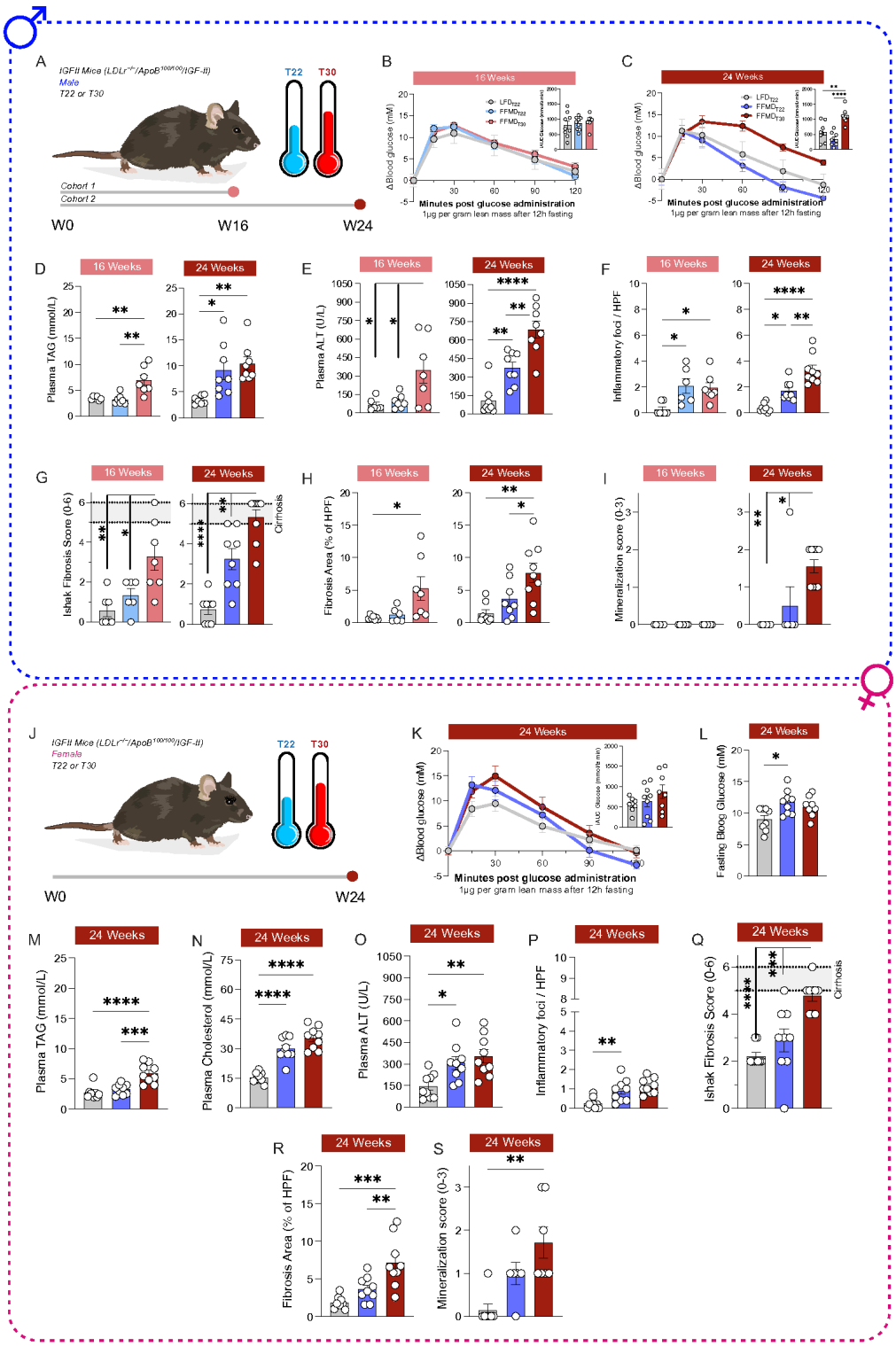


Figure 2

Thermoneutrality potentiates cardiohepatic disease in male (A-I) and female (J-S) LDLr$^{-/-}$/ApoB$^{100/100}$/IGF-II (IGFII) mice. (A) Study design of the male IGFII experiment dissecting the influence of different ambient temperatures on cardiometabolic disease. Change in blood glucose levels after an oGTT after 16 weeks (B) and 24 weeks (C), including area-under-the-curve (AUC) analysis. Data are shown as mean ± SEM. Plasma measurements of TAG (D) and ALT (E) after 16 or 24 weeks, shown as

the mean ± SEM. (F) Average number of inflammatory foci of >5 immune cells per high-power field (HPF), shown as the mean ± SEM. (G) Ishak histological fibrosis grading, shown as the mean ± SEM. The grey shaded area of 5-6 indicates range of cirrhosis. (H) Fibrotic area quantified as red stained collagen tissue per HPF, shown as the mean ± SEM. (I) Aortic mineralization score following a Micro-computed tomography (μCT) scan, shown as the mean ± SEM. (J) Study design of the female IGFII experiment dissecting the influence of different ambient temperatures on cardiometabolic disease after 24 weeks. Change in blood glucose levels after an oGTT at 24 weeks (K), including AUC analysis. Data are shown as mean ± SEM. (L) Fasting blood glucose levels, shown as the mean ± SEM. Plasma measurements of TAG (M) and cholesterol (N) after 24 weeks, shown as the mean ± SEM. (O) Plasma ALT levels, shown as the mean ± SEM. (P) Average number of inflammatory foci of >5 immune cells per HPF, shown as the mean ± SEM. (Q) Ishak histological fibrosis grading, shown as the mean ± SEM. (R) Fibrotic area per HPF, shown as the mean ± SEM. (S) Aortic mineralization score, shown as the mean ± SEM. N = 8-9 per group, with individual data points representing each mouse. Data were analysed with a one-way ANOVA with Tukey's multiple comparison test. Statistical significance was considered at $p < 0.05$, where * = $p < 0.05$, ** = $p < 0.01$, *** = $p < 0.001$, **** = $p < 0.0001$.

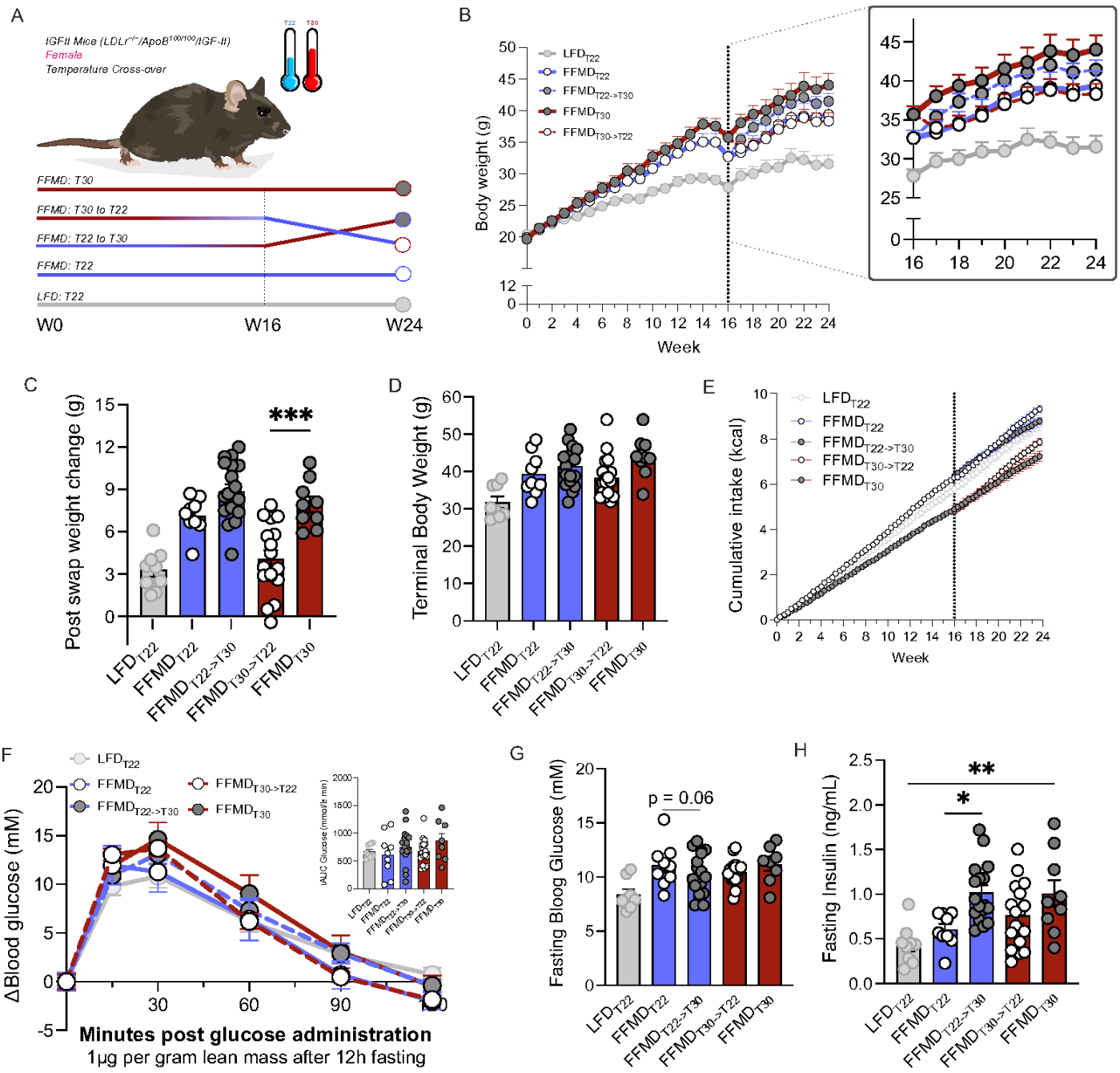


Figure 3

Ambient temperature shows minimal impact on glucoregulatory function in a controlled crossover study in IGFII female mice. (A) Schematic of study design showing which groups change temperature after 16 weeks of FFMD-feeding for the final 8 weeks. Body weight development throughout the entire study (B), with cumulative weight gain after temperature swap (C) and total terminal body weight (D), shown as the mean ± SEM. (E) Cumulative kilocalorie (kcal) intake during the course of the study, shown as the mean ± SEM. (F) Change in blood glucose after an oGTT with AUC analysis shown as the mean ± SEM. Dotted lines indicate temperature swapped groups. Fasting levels of blood glucose (G) and plasma

insulin (H) shown as the mean ± SEM. N = 8-9 per temperature-constant group and 17-18 in temperature-swapping groups, with individual data points representing each mouse. Grey filled dots indicate groups housed at T30 at termination. Data were analysed with a one-way ANOVA with Tukey's multiple comparison test. Statistical significance was considered at $p < 0.05$, where * = $p < 0.05$, ** = $p < 0.01$, *** = $p < 0.001$, **** = $p < 0.0001$.

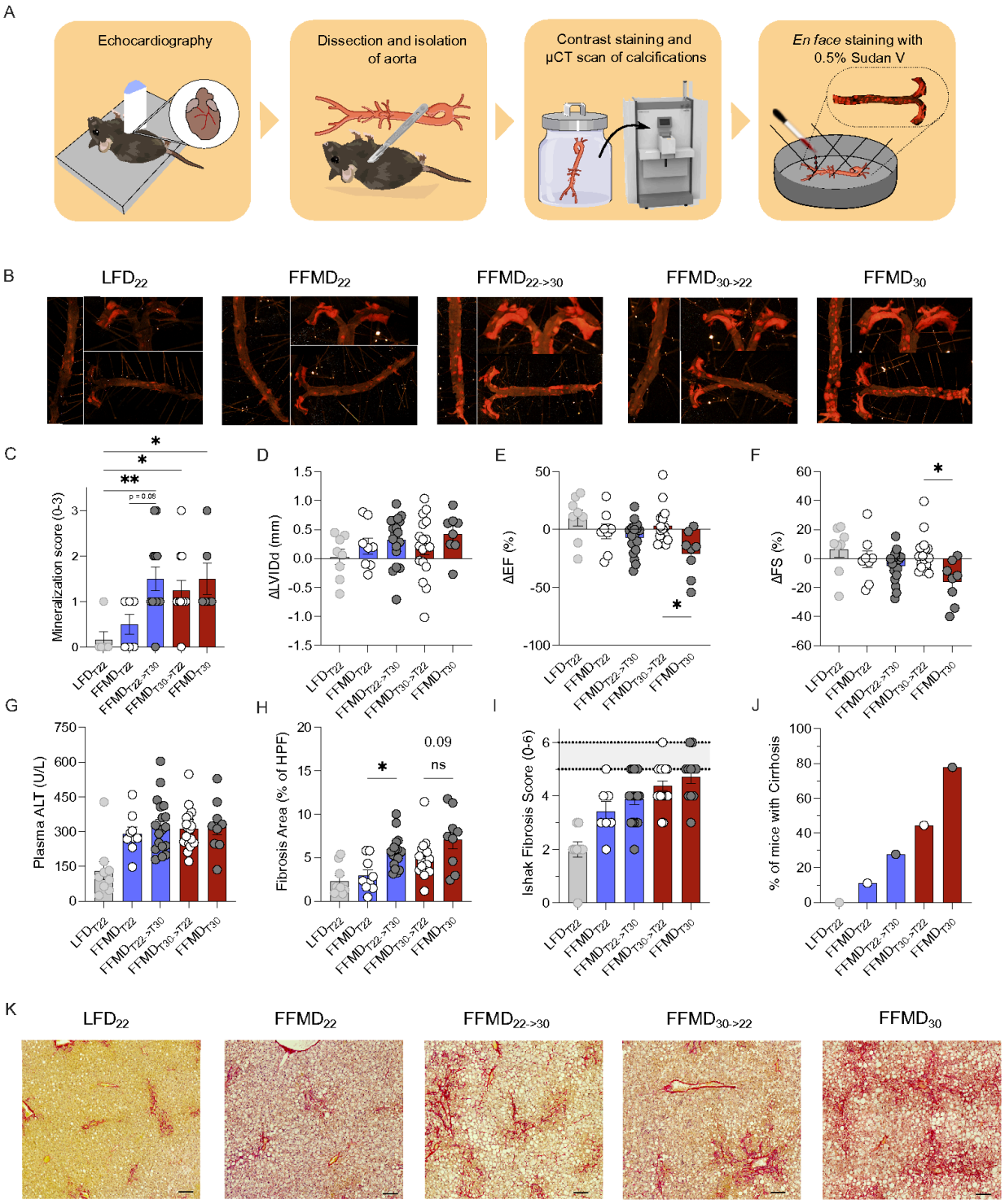


Figure 4

Ambient temperature dictates cardiometabolic disease severity. (A) Graphical representation of interrogation of the cardiac phenotype of IGFII female mice of the crossover study. Mice were subjected to echocardiography before termination. Subsequently, careful dissection of the entire aorta was followed by submersion in contrast agent and μCT scan. After μCT scan aortas were carefully opened subjected to *en face* staining with 0.5% Sudan V agent for visual inspection of lesions. (B) Representative *en face* stainings of aortas from each group. (C) Aortic mineralization scores following μCT scans, shown as the mean ± SEM. Echocardiographic measurements showing change in Left Ventricular Internal Diameter at end-diastole (ΔLVIDd; D), ejection fraction (ΔEF; E), and fractional shortening (ΔFS; F), shown as the mean ± SEM. (G) Plasma ALT levels, shown as the mean ± SEM. (H) Fibrosis area per HPF, shown as the mean ± SEM. Ishak fibrosis grading (I), shown as the mean ± SEM, and total percent of mice developing frank cirrhosis (J). (K) Representative histology pictures of sirus red stained livers, scale bars = 100μm. N = 8-9 per temperature-constant group and 17-18 in temperature-swapping groups, with individual data points representing each mouse. Grey filled dots indicate groups housed at T30 at termination. Data were analysed with a one-way ANOVA with Tukey's multiple comparison test. Statistical significance was considered at $p < 0.05$, where * = $p < 0.05$, ** = $p < 0.01$, *** = $p < 0.001$, **** = $p < 0.0001$.

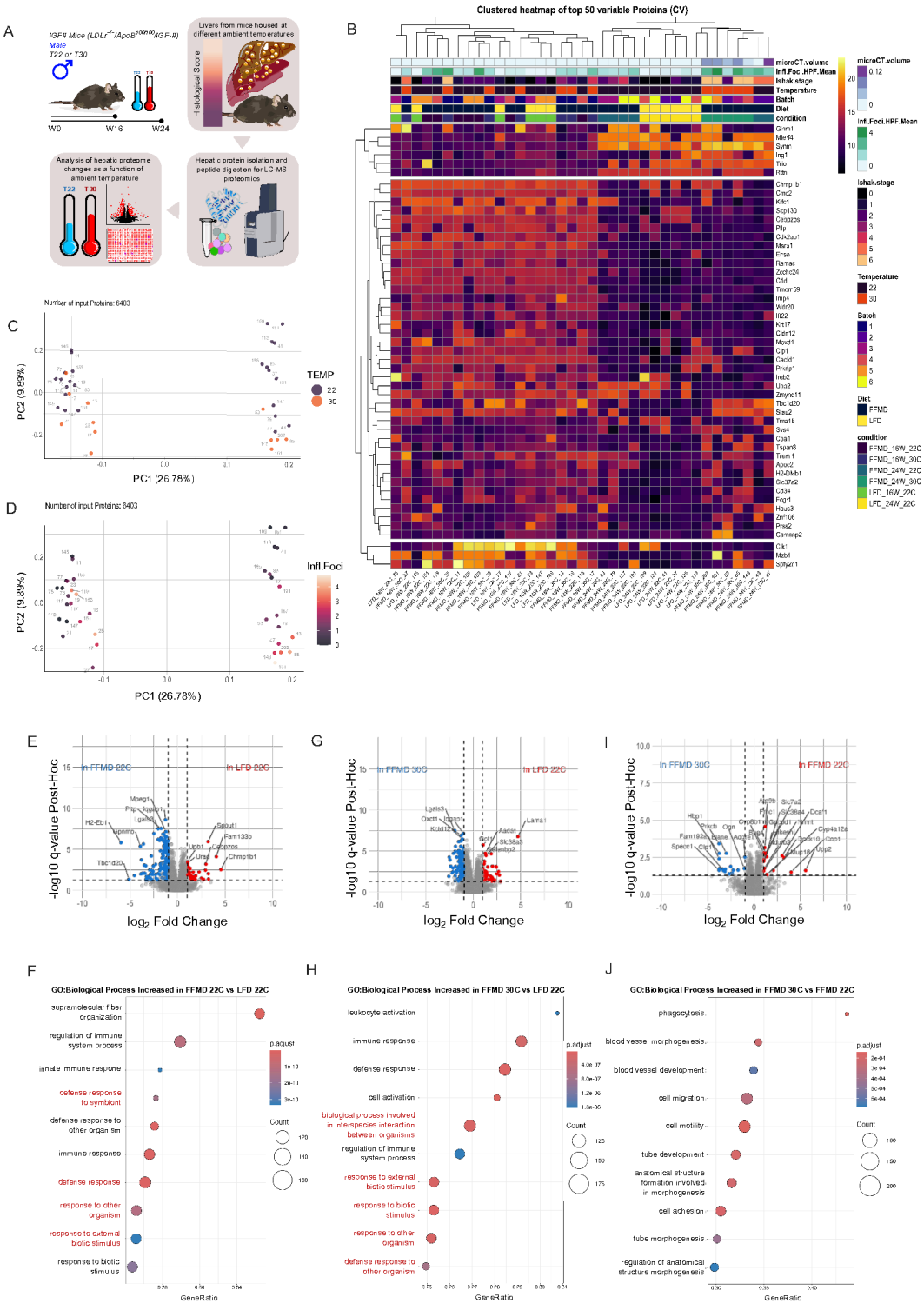


Figure 5

Liver proteomics analysis of male IGFII mice highlights processes involved in fibrosis and immune response towards microorganisms. (A) Schematic of workflow. (B) Clustered heatmap of top 50 most variable proteins with indicators of experimental variables. Principal component analysis (PCA) plots of data variance associated with ambient temperature (C) and degree of hepatic inflammation (D). (E) Volcano plot of proteins associated with FFMD-fed mice at T22 compared to low-fat diet (LFD) fed mice,

with specific Gene Ontology Biological Processes (GO:BP) highlighted in (F). (G) Volcano plot of proteins associated with FFMD-fed mice at T30 compared to LFD-fed mice, with specific GO:BPs highlighted in (H). (I) Volcano plot of proteins associated with FFMD-fed mice at T30 versus T22, with specific GO:BPs highlighted in (J).

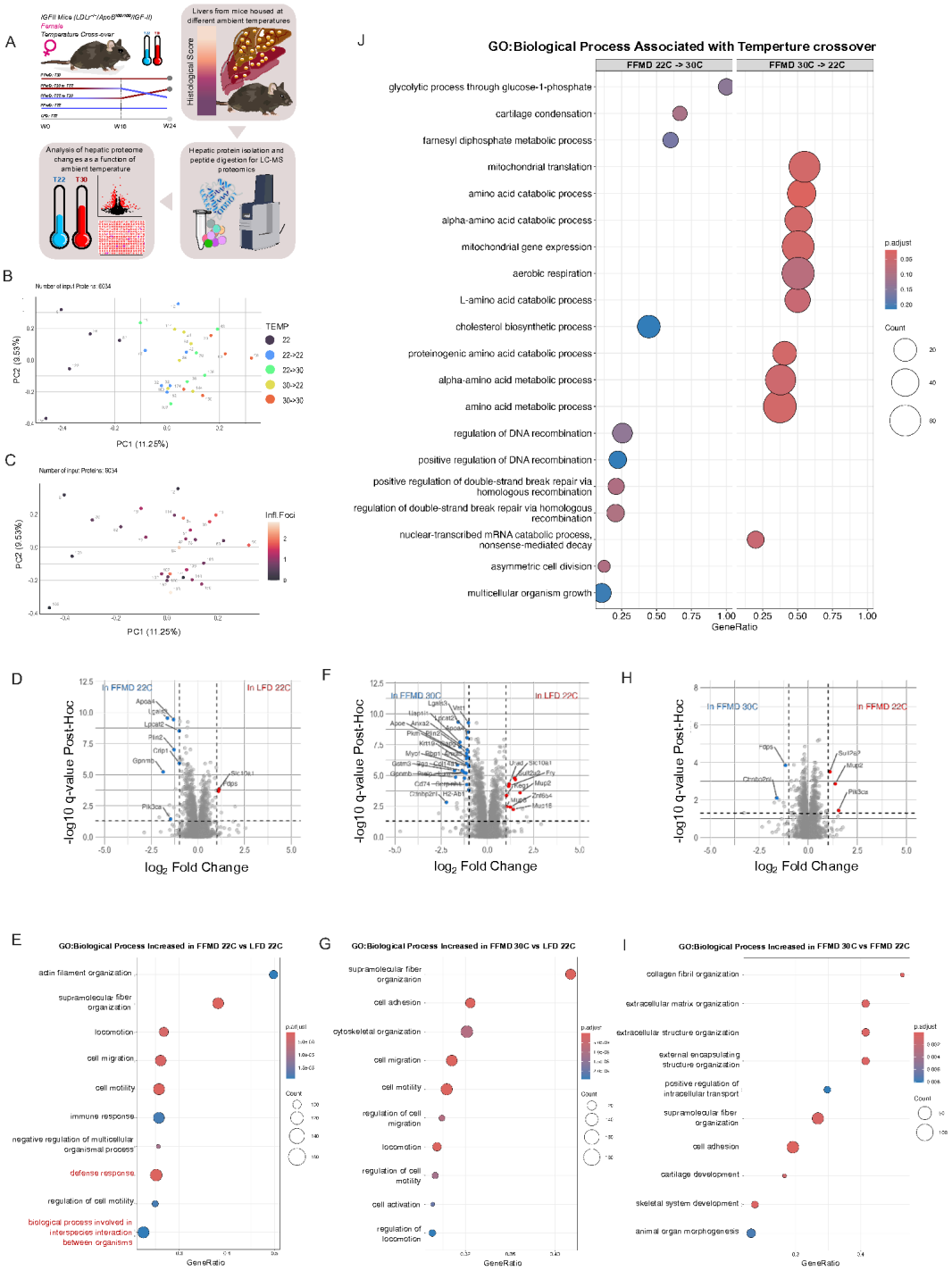


Figure 6

Ambient temperature dictates mitochondrial health and DNA repair. (A) Schematic of workflow. Principal component analysis (PCA) plots of data variance associated with ambient temperature (B) and degree of hepatic inflammation (C). (D) Volcano plot of proteins associated with FFMD-fed mice at T22 compared to low-fat diet (LFD) fed mice, with specific GO:BPs highlighted in (E). (F) Volcano plot of proteins associated with FFMD-fed mice at T30 compared to LFD-fed mice, with specific GO:BPs highlighted in (G). (H) Volcano plot of proteins associated with FFMD-fed mice at T30 versus T22, with specific GO:BPs highlighted in (H). (J) GO:BPs associated with swapping ambient temperature from T22->T30 and T30->T22.

Supplementary Files

This is a list of supplementary files associated with this preprint. Click to download.

- 4Jensenetal.T2DMASLDCVDaxisReportingSummary.pdf
- 5Jensenetal.T2DMASLDCVDaxisSupplementaryinformation.pdf